Published in final edited form as:
IEEE Trans Ultrason Ferroelectr Freq Control. 2014 December ; 61(12): 1976–1987. doi:10.1109/TUFFC.2014.006362.

Spatial coherence in human tissue: implications for imaging and measurement

Gianmarco Pinton, **Gregg Trahey**, and **Jeremy Dahl**

Abstract

The spatial coherence properties of the signal backscattered by human tissue and measured by an ultrasound transducer array are investigated. Fourier acoustics are used to describe the propagation of ultrasound through a model of tissue that includes reverberation and random scatterering in the imaging plane. The theoretical development describes how the near-field tissue layer, transducer aperture properties, and reflectivity function at the focus reduce the spatial coherence of the imaging wave measured at the transducer surface. Simulations are used to propagate the acoustic field through a histologically characterized sample of the human abdomen and to validate the theoretical predictions. *In vivo* measurements performed with a diagnostic ultrasound scanner demonstrate that simulations and theory closely match the measured spatial coherence characteristics in the human body across the transducer array's entire spatial extent. The theoretical framework and simulations are then used to describe the physics of spatial coherence imaging, a type of ultrasound imaging that measures coherence properties instead of echo brightness. The same echo data from an F/2 transducer was used to generate B-mode and short lag spatial coherence images. For an anechoic lesion at the focus the contrast to noise ratio is 1.21 for conventional B-mode imaging and 1.95 for spatial coherence imaging. It is shown that the contrast in spatial coherence imaging depends on the properties of the near-field tissue layer and the backscattering function in the focal plane.

I. Introduction

The spatial coherence of a wave is a measure of how it changes as a function of distance. For example, a plane wave is spatially coherent along the axis that is perpendicular to the direction of propagation because it is self-similar at each point on the axis. However if that wave is reflected by a random mirror that scrambles the amplitude and the phase at each point then the wave becomes incoherent, i.e. the wave is no longer self similar along the axis. More precisely, the definition of coherence is related to the shape of the statistical autocorrelation function of the wave. The variation in the autocorrelation as a function of the distance between two points measures whether a process is coherent (if the function is wide) or incoherent (if it is narrow) [1].

Further author information: Send correspondence to G. Pinton: pinton@dalembert.upmc.fr.

In the 1930's Zernike established a theoretical framework that described partial coherence and how the coherence of the wave field evolves with propagation [2]. One of the first uses of spatial coherence in acoustics was in pulse-echo ultrasound in the 1990's [3], [4] when a fundamental theorem of statistical optics, the Van Cittert-Zernike (VCZ) theorem [2], [5], was applied to acoustic waves. The theorem predicts the spatial coherence of the pressure field backscattered by a random medium and observed by an ultrasound transducer array. This theoretical tool answers a basic question: how similar are signals measured by an ultrasound transducer array as a function of space? Since then, the study of spatial coherence in ultrasound has been applied to aberration correction, speckle reduction, defect detection, and more recently spatial coherence imaging.

Speckle reduction, for example, relies on incoherent processing to improve ultrasound image quality. For example, a backscattered field can be measured by multiple small coherent subapertures and after envelope detection the individual signals can be combined to remove phase sensitivity from the imaging process [6], [7]. The improvement in speckle signal to noise ratio (SNR) decreases as the spatial coherence of the backscattered field widens [3]. The spatial coherence of backscattered ultrasound can also be used to describe degree of aberration from an ideally focused beam or the focusing quality of ultrasound [8], [9]. It has furthermore been demonstrated that the spatial coherence function narrows as the aberration increases [7].

It has been shown that the spatial coherence properties of backscattered ultrasound can provide information on the statistical structure of the medium and more specifically can be used to detect defects in fully or partially incoherent media, and in media with anisotropic scatterer distributions [10], [11].

Spatial coherence has also been utilized in direct imaging applications [12], [13]. Lediju et al. [12] proposed a display of backscattered ultrasound based on the integration of the spatial coherence function over the short-lag region. The proposed method, called short-lag spatial coherence (SLSC) imaging, yields bright pixel values in regions where there is partial or high-coherence, and dark values where there is low or no coherence in the backscattered wavefronts. Specifically, regions of tissue or speckle-generating targets typically exhibit bright pixel values, while noise and reverberation generate dark pixel values.

The objectives of this paper are to establish a theoretical description of spatial coherence in human tissue and its implications for spatial coherence ultrasound imaging. To establish a physical description of coherence imaging, we extend the formalism initially developed by Zernike to pulse-echo ultrasound in a model of tissue. In particular, Fourier acoustics are used to describe the spatial coherence of an acoustic wave as it propagates through a model of the human abdomen that includes aberration and reverberation of the acoustic wave.

This model is compared to *in vivo* spatial coherence functions of the human abdomen and with simulations of the spatial coherence of the backscattered ultrasound signal in realistic diagnostic imaging conditions. The backscattered field is determined with a finite difference time domain Full-wave nonlinear acoustic (Fullwave) simulation that includes multiple

scattering and reverberation clutter [14]. The Fourier acoustics model and simulations demonstrate the physical mechanisms involved in spatial coherence imaging.

A schematic representation of a pulse echo measurement performed by a single transducer is shown on the right of Fig. 1. After the pulse is emitted, part of the wave is reflected in the near field tissue layers where it reverberates. This is an additive source of acoustic noise that persists throughout the measurement. Reverberations have been shown to be a significant cause of image quality degradation and are the principal reason why harmonic ultrasound imaging is better than fundamental imaging [14], [16]. In this paper we address questions such as, how do the near-field tissue layer, aperture properties, and reflectivity at the focus affect the spatial coherence of the wave measured in the focal plane?

II. Definition of coherence

Spatial coherence is defined here as the statistical autocorrelation function of the field at two points x_1 and x_2. For a random process, $\psi(x)$, the expected statistical autocorrelation can be written as

$$R_{\psi\psi}(x_1, x_2) = E\{\psi(x_1)\psi^*(x_2)\} \quad (1)$$

where E is the ensemble average, and * is the complex conjugate. If ψ is stationary with respect to space, then the autocorrelation depends only on the distance $\Delta x = x_2 - x_1$. If the autocorrelation function $R(\Delta x)$ is narrow then the process is incoherent and if it is wide then it is coherent. The wavefront of a short pulse emitted by a multi-element ultrasound transducer propagating through a scattering medium such as tissue, is initially coherent. However its reflection, which is the product of the incident wave with the scatterer distribution, amplitude, and directivity pattern, is only partially coherent.

The spatial coherence between two signals s received from an ultrasound transducer array can be estimated by a time-windowed, normalized correlation function r, which determines the resemblance between signals:

$$r(x_1, x_2) = \frac{\int_\tau s(x_1, t)s(x_2, t)dt}{\sqrt{\int_\tau s^2(x_1, t)dt \int_\tau s^2(x_2, t)dt}} \quad (2)$$

where τ defines the time interval over which the coherence is measured. The relationship between the time domain description in Eqn. 2 and the frequency domain description in Eqn. 1 has been shown to be [4]

$$E\{r(x_1, x_2)\} = \int_{\text{bandwidth}} R^{\omega}_{\psi\psi}(x_1, x_2)d\omega \quad (3)$$

where the statistical autocorrelation at a particular frequency ω is written as $R^{\omega}_{\psi\psi}$. A version of Eqn. 2 can be defined for use with the discrete data obtained from ultrasound scanners and acoustic simulations. If s_i is the signal received by the ith element of a transducer (at position x_i), then the correlation is given by

$$\rho(x_i, x_j) = \frac{\sum_{n=N}^{M} [s_i(n) - \bar{s}_i][s_j(n) - \bar{s}_j]}{\sqrt{\sum_{n=N}^{M} [s_i(n) - \bar{s}_i]^2 \sum_{n=N}^{M} [s_j(n) - \bar{s}_j]^2}} \quad (4)$$

where n is the discrete time index, N and M define the temporal window over which the correlation is performed, and $\bar{s}_i$ is the average of the signal over the window length. This window is used to select a specific depth of interest (e.g. the focal depth). The normalization ensures that the measure is independent of the relative strength of the received echo signals. For a stationary field, the autocorrelation depends only on the distance between points x_i and x_j. Therefore to determine the correlation value as a function of the inter-element distance or lag, an average is performed over all x_i, x_j such that $x_j - x_i = \Delta x$:

$$\rho(\Delta x) = \frac{1}{K - m} \sum_{i=1}^{K-m} \rho(x_i, x_{i+m}) \quad (5)$$

where K is the number of elements in the transducer. Thus for an inter-element distance of 1, the average is performed over $K - 1$ values, and for an inter-element distance of $K - 1$, there is one estimate.

III. Model for a focused ultrasound transducer and tissue with reverberation clutter

The derivation of the spatial coherence of the acoustic wave field is shown in full in the appendix. It is based on the framework set out by Derode *et al.* for defect detection in anisotropic media [17] but it has been extended to include aberration and reverberation clutter. In this section previous results are summarized and the extension to reverberation clutter is shown in full.

Fig. 2 shows a schematic representation of the Fourier acoustic model and establishes a coordinate system with the transducer at the $z = 0$ plane and the focal plane at a depth of F. The acoustic field propagates from the transducer plane to the focal plane where the pulse is reflected and then propagates back to the transducer plane. In this model the signal's phase and amplitude can be modified at three locations: 1) the transmitting aperture, 2) the focal plane, and 3) the receiving aperture.

Table I summarizes the variables and mathematical notation used throughout the paper.

The transmittance function T can be used to describe the shape of the transducer, apodization, focusing geometry. In the case of thin near-field aberrators, it can also describe aberration functions. The transmittance function can include kerf, apodization, and any other arbitrary phase/amplitude functions that are restricted to the transducer plane.

For example, a typical imaging transducer has a rectangular aperture. For a rectangular transducer of size $a \times b$, define $O(x, y)$ in the $z = 0$ plane as:

$$O(x,y)=\text{rect}\left(\frac{x}{a}\right)\text{rect}\left(\frac{y}{b}\right) \quad (6)$$

where rect is the rectangular function is defined as

$$\text{rect}=\begin{cases}1 & \text{if}|x|<1/2\\ 0 & \text{else}\end{cases} \quad (7)$$

Here we will define two phase functions. The first is a thin lens with a radius of curvature F that describes a wave that converges to the point $z = F$ on the propagation axis. The second is a thin screen model of tissue aberration, the complex function $A(x, y)$, which is based on the assumption that the distributed variations in the speed and amplitude of sound can be approximated by phase and amplitude aberration in a single plane at the transducer surface. This assumption is less accurate than the simulations which include a distributed aberrator, however it can be easily included in the theory. The aberration function can be defined, for example, in terms of the root mean square amplitude of the phase variation and the characteristic spatial correlation lengths in the x and y directions. These depend respectively on the amplitude of the speed of sound variations and the spatial distribution of the aberrators (the tissue's structure and geometry). If the aberration only modifies the phase, then $|A| = 1$ uniformly, and if the aberration only modifies the amplitude, then $\arg(A) = 0$ uniformly.

The total transmittance function of the aperture is thus

$$T(x,y)=O(x,y)A(x,y)e^{-j(\pi/\lambda F)(x^2+y^2)} \quad (8)$$

The quadratic term in Eqn. 8 represents a parabolic focusing function that approximates a spherically converging wave within Fresnel's approximation [5].

In section VIII-A the transmittance function $T(x, y)$ is used to calculate propagation from the source plane to a depth z with a convolution with the propagation operator. The field at the focus, $U_z(X, Y)$, can be expressed as a Fourier transform of the aperture:

$$U_z(X,Y)=\frac{1}{\lambda z}e^{j(\pi/\lambda z)(X^2+Y^2)}\text{FT}_{2\text{D}}\{\tilde{T}(x,y)\}_{(X/\lambda z,Y/\lambda z)} \quad (9)$$

The modified transmittance function $\tilde{T}$, defined in the Appendix by Eqn. 27, describes both the transmittance and focusing. Section VIII-B describes how the field at the imaging plane is reflected at depth z by the function $\chi(X, Y)$. To model a random scatterer distribution this function can be described as a random mirror, i.e. a thin layer of scatterers that randomly change the phase of the reflected signal. The reflected field is then

$$U_z^{\text{refl}}(X,Y)=\chi(X,Y)U_z(X,Y) \quad (10)$$

A. Propagation from z to 0

To calculate the field received at the transducer face, $\psi_\omega(x, y)$ the field at z must propagate back to 0, which is obtained by a convolution of the reflected field with the propagation operator h_z and a multiplication with the transmittance function. Multiple reflections, such as reverberation from tissue in the near field, is modeled as an additive source at the transducer surface and is defined by the function $\mathcal{M}(x, y)$. This is an additive source that extends across the transducer face for all time. The received field is then

$$\psi_\omega(x,y)=T(x,y)\left(U_z^{\mathrm{refl}}\underset{xy}{**}h_z\right)+\mathcal{M}(x,y)=\frac{1}{\lambda^2 z^2}T(x,y)e^{j(\pi/\lambda z)(x^2+y^2)}\iint e^{j(2\pi/\lambda z)(X^2+Y^2)}e^{-j(2\pi/\lambda z)(Xx+Yy)}\tilde{\Omega}(X,Y)\chi(X,Y)dXdY+\mathcal{M}(x,y) \quad (11)$$

where $\tilde{\Omega}$ is the beam profile defined by

$$\tilde{\Omega}(X,Y)=\mathrm{FT}_{2\mathrm{D}}\{\tilde{T}(x,y)\}_{(X/\lambda z,Y/\lambda z)} \quad (12)$$

The first term under the integral in Eq. 11 can be simplified. The beam intensity at z is proportional to $|\tilde{\Omega}(X, Y)|^2$ and Eqn. 12 describes the beam's spatial distribution (without the $e^{j(2\pi/\lambda z)(X^2+Y^2)}$ phase and $1/\lambda z$ constant in Eqn. 26). In the far field the phase varies slowly with respect to the beam's spatial extent, defined here as l. The Fraunhofer approximation can be used to simplify the description of the field at z. In particular, if $l^2 \ll \lambda z$, then $e^{j(2\pi/\lambda z)(X^2+Y^2)} \approx 1$ over the beam's spatial extent in the X–Y plane. For a focused unaberrated transducer, $l = \lambda F/a$, which implies that in the $z \approx F$ zone $l \ll a$, i.e. the focal spot is much smaller than the aperture size. Phase and amplitude aberration enlarge the focal spot. Therefore the function $O(x, y)$ must be sufficiently large so that the focal spot is still much smaller than the aperture size. This condition is met in the focal zone for the majority of diagnostic imaging configurations.

The integral in Eqn. 11 can then be expressed as a Fourier transform and the backscattered field can be written as

$$\psi_\omega(x,y)=\frac{1}{\lambda^2 z^2}\tilde{T}(x,y)\mathrm{FT}_{2\mathrm{D}}\{\tilde{\Omega}(X,Y)\chi(X,Y)\}_{(x/\lambda z,y/\lambda z)}+\mathcal{M}(x,y) \quad (13)$$

Eqn 13 is the total field received at the transducer with the effects of phase and amplitude aberration and multiple scattering, and it can be used to calculate the spatial coherence of the backscattered field.

B. The autocorrelation of the backscattered field

Denote $E_\chi\{\}$ as the ensemble average over multiple random mirror realizations and $E_{\mathcal{M}}\{\}$ as the ensemble average over multiple reverberating scatterer realizations. We assume that the reflections from the focal plane are independent and decorrelated from the reverberations in the near field. The correlation $R^{\omega}_{\psi\psi}$ between two monochromatic signals at positions (x_1, y_1) and (x_2, y_2) is

$$R^{\omega}_{\psi\psi}(x_1,x_2,y_1,y_2) = E_{\mathscr{M}}\{E_{\chi}\{\psi_{\omega}(x_1,y_1)\psi^{*}_{\omega}(x_2,y_2)\}\} = E_{\mathscr{M}}\{E_{\chi}\{(\frac{1}{\lambda^2 z^2}\tilde{T}(x_1,y_1)\mathrm{FT}_{2\mathrm{D}}\{\tilde{\Omega}(X_1,Y_1)\chi(X_1,Y_1)\}_{(x_1/\lambda z,y_1/\lambda z)} + \mathscr{M}(x_1,y_1))(\frac{1}{\lambda^2 z^2}\tilde{T}^{*}(x_2,y_2)\mathrm{FT}_{2\mathrm{D}}\{\tilde{\Omega}(X_2,Y_2)\chi(X_2,Y_2)\}_{(x_2/\lambda z,y_2/\lambda z)} + \mathscr{M}(x_2,y_2))^{*}\}\} \quad (14)$$

Since the signals from $\chi(X, Y)$ and $\mathscr{M}(x, y)$ are decorrelated, the cross terms from the multiplication in the curly brackets of Eqn. 14 vanish and

$$R^{\omega}_{\psi\psi}(x_1,x_2,y_1,y_2) = \frac{1}{\lambda^4 z^4}\tilde{T}(x_1,y_1)\tilde{T}^{*}(x_2,y_2)[E_{\mathscr{M}}\{E_{\chi}\{\mathrm{FT}_{2\mathrm{D}}\{\tilde{\Omega}(X_1,Y_1)\chi(X_1,Y_1)\}_{(x_1/\lambda z,y_1/\lambda z)}\mathrm{FT}_{2\mathrm{D}}\{\tilde{\Omega}^{*}(X_2,Y_2)\chi^{*}(X_2,Y_2)\}_{(x_2/\lambda z,y_2/\lambda z)}\}. \quad (15)$$

By reorganizing the autocorrelations and Fourier transforms and this can be further simplified to

$$R^{\omega}_{\psi\psi}(x_1,x_2,y_1,y_2) = \frac{1}{\lambda^4 z^4}\tilde{T}(x_1,y_1)\tilde{T}^{*}(x_2,y_2)[\mathrm{FT}_{4\mathrm{D}}\{\tilde{\Omega}(X_1,Y_1)\tilde{\Omega}^{*}(X_2,Y_2)R_{\chi\chi}(X_1,X_2,Y_1,Y_2)\}_{(x_1/\lambda z,x_2/\lambda z,y_1/\lambda z,y_2/\lambda z)}] + R_{\mathscr{M}\mathscr{M}}(x_1,x_2,y_1,y_2) \quad (16)$$

This expression shows that the spatial coherence is a linear combination of reverberations in the near field and scattering from the mirror in the focal plane if the two are decorrelated. It can be shown that this expression reduces to the VCZ theorem when the aberrating function is neglected by setting $A = 1$, $\mathscr{M} = 0$, and $\chi(X, Y)$ is a stationary random process. By using the correlation theorem for the Fourier transform, by noting that $\mathrm{FT}_{2\mathrm{D}}\{\tilde{\Omega}(X, Y)\}_{(x/\lambda z,y/\lambda z)} = \lambda^2 z^2\, \tilde{T}(x, y)$, and by assuming that $\tilde{T}$ is an even function Eqn. 16 can be re-written in a form that is similar to the classical definition of the VCZ theorem:

$$R^{\omega}_{\psi\psi}(x_1,x_2,y_1,y_2) = \frac{1}{\lambda^2 z^2}\tilde{T}(x_1,y_1)\tilde{T}^{*}(x_2,y_2)[\tilde{T}(x_1,y_1)\tilde{T}^{*}(x_2,y_2) \underset{x_1 x_2 y_1 y_2}{****}\mathrm{FT}_{4\mathrm{D}}\{R_{\chi\chi}(X_1,X_2,Y_1,Y_2)\}_{(x_1/\lambda z,x_2/\lambda z,y_1/\lambda z,y_2/\lambda z)}] + R_{\mathscr{M}\mathscr{M}}(x_1,x_2,y_1,y_2) \quad (17)$$

Eqns. 16, 17 are generalized forms of the VCZ theorem that takes into account arbitrary aperture functions, phase screen aberration, and reverberations. Several cases demonstrating these effects will be investigated with simulations and measurements in the following sections.

IV. Full-wave nonlinear acoustic simulation

To determine the acoustic field at the element locations, the finite difference Fullwave code was used to propagate a diagnostic ultrasound pulse through a measured representation of human abdominal tissue[14]. Data for the abdominal layer was obtained from a study that characterized cross-sections of the human abdomen [15]. Each slice was histologically stained to identify three types of tissue: connective, muscle, and fat. To convert this data set

to acoustical maps, each of these types is assumed to have constant material properties (speed of sound, density, attenuation, and nonlinearity). This data set has been previously used with the Fullwave program. The details of this acoustic conversion are the same as those found in the reference [14] and they are briefly summarized below.

The speed of sound map is shown on the left of Fig. 1 (not shown are the maps for density, attenuation, and nonlinearity). The skin is found in the first 2mm thick layer. From 2 to 17 mm there is fat with a low speed of sound and each globule is surrounded by a thin layer of connective tissue with a high speed of sound. Between 17 and 21 mm there is a layer of muscle tissue (high speed of sound) with fat striations (low speed of sound). The impedance mismatch between these regions generates areas of reverberation that trap ultrasound. The histological measurements end at 21 mm. A region of homogeneous liver tissue is modeled beneath the muscle layer in the simulation. Cells and sub-cellular structures, such as organelles, are too small to have been measured optically. However, they play an important role in scattering ultrasound. Therefore subresolution scatterers are added in the simulations with a density of 20 per resolution cell, and a mean separation of 335 μm.

A 1.5 cycle circularly focused pulse with a center frequency of 2.1 MHz and was emitted by a 2.5 cm wide F/2 transducer focused at 5 cm depth with 192 equally spaced elements. The signals that are received by an ultrasound transducer are time-delayed according to the circular focusing geometry before the spatial coherence is calculated.

The full-wave equation that models propagation is a second order wave equation that describes a nonlinear wave propagating in an attenuating medium [14]. In the following simulations the spatial grid was fixed at 45 μm with a time step corresponding to a Courant-Friedrichs-Lewy (CFL) condition of 0.2 relative to a propagation speed of 1540 m/s. Since there is no added benefit to verifying the physics in three dimensions but the computational cost is higher he simulations were performed in two dimensions. These simulations were written with custom MPI and C code and they run on a Linux cluster. This simulation tool includes the effects of reflection, scattering, and reverberation that are necessary to correctly model the coherence lengths of ultrasonic signals.

To verify that the Fullwave simulation follows the basic prediction of the VCZ theorem for a focused transducer, the random mirror χ is modeled as a randomly distributed field of scatterers with a constant average density and a cross section of 40 μm. The background acoustic field has a speed of sound of 1540 m/s, a density of 1000 kg/m^3 and an attenuation of 0.3 dB/MHz/cm. The scatterer distribution is randomly distributed in space and amplitude, with an impedance mismatch that varies between 0 and 5% of the background impedance. This weak impedance mismatch ensures that scattering events are predominantly single (rather than multiple). The scatterer distribution and speed of sound map for this simulation is illustrated on the left of Fig. 3.

To determine the spatial coherence curve for the Fullwave simulation, the signals recorded with a 40 MHz sampling frequency at each element were spherically delayed to focus at 5 cm depth (note that here $z = F = 5$ cm). The signals were then windowed at the focus with a window length of 2λ. The average spatial correlation as a function interelement distance

(expressed as a fraction of the total aperture width) was calculated according to Eqn. 5 and is plotted as the dashed curve in Fig. 3. This procedure was repeated for 10 independent scatterer realizations to obtain error bars. Each transmit receive simulation took 1 hour per CPU.

Spatial coherence curves were calculated for different cases that represent varying spatial coherence conditions. In particular, these cases are: propagation through a field of distributed sub-resolution random scatterers, propagation through the abdominal layer without sub-resolution scatterers, propagation through sub-resolution scatterers and the abdominal tissue, and propagation through abdominal layers with an artificially modified impedance mismatch. Lastly conventional B-mode images are compared to images generated with short-lag spatial coherence (SLSC) values.

The simulation process follows the same acoustic sequence as a physical ultrasound transducer. First, each of the elements in the transducer emit a time delayed pulse with a spherically focused profile. Next, the sound propagates through the heterogeneous medium and is reflected by scatterers. Finally, the sound that travels back to the surface of the transducer elements is recorded and stored for processing. These simulation results are compared to *in vivo* liver data acquired with a commercial ultrasound scanner.

V. Examples

A. Uncluttered and unaberrated wavefield

For an aberrating function that changes neither the amplitude nor the phase ($A \equiv 1$) and has zero additive reverberation clutter signal ($\mathscr{M} \equiv 0$), Eqn 17 can be simplified to the well-known VCZ theorem. At a depth of $z = F$, the phase from the emitted field is aligned in the focal plane (cf. Eqn. 27) and

$$\tilde{T}(x,y)=O(x,y)=\text{rect}\left(\frac{x}{a}\right)\text{rect}\left(\frac{y}{b}\right) \quad (18)$$

Here O describes the masking function for the transducer.

Furthermore, if the random mirror in the focal plane is fully incoherent so that each point has a reflection function with a phase and amplitude that are independent from its neighbors, then

$$R_{\chi\chi}(\Delta X,\Delta Y) \propto \delta(\Delta X)\delta(\Delta Y) \quad (19)$$

For the sake of simplicity we will consider only the first dimension, x. It then follows that Eqn. 17 simplifies to

$$R^{\omega}_{\psi\psi}(\Delta x) \propto \frac{1}{\lambda^2 z^2}\text{rect}\left(\frac{x}{a}\right) \underset{\Delta x}{*} \text{rect}\left(\frac{x}{a}\right) = \frac{1}{\lambda^2 z^2}\text{tri}\left(\frac{\Delta x}{a}\right) \quad (20)$$

This confirms a well known result: for a rectangular transducer the spatial coherence function measured at the transducer face decreases linearly as a triangle function, tri, whose width is double that of the transmit aperture [3]. This function is plotted in solid black on the

right image of Fig. 3. The simulated spatial coherence and theoretical predictions shown in Fig. 3 are in good agreement and within the error bars.

The scatterers in Fig. 3 are distributed throughout all depths from 0 to 6 cm rather than being confined to a depth of 5 cm. This is physically realistic with respect to modeling tissue but it is a departure from the random mirror model. Since the medium is weakly or singly scattering and a time gate can be used to select the signal reflected from the focus to meet the thin random mirror conditions. Nevertheless, the scatterers near the transducer are a source of uncorrelated weak multiple scattering, which may slightly reduce the correlation observed in the simulation curve.

B. Reverberation clutter

The reverberation clutter, $\mathcal{M}$, cannot be measured directly *in vivo* because it is inseparable from the signal that is reflected from the random mirror. We have previously shown that reverberation clutter has a short correlation length [13]. Here the acoustic field from reverberation clutter, $\mathcal{M}$, can be calculated directly with simulations by removing the random mirror. The simulated acoustic map is therefore identical to the map shown in Fig. 1: the map of tissue structure without sub-resolution scatterers. Since there is no sound reflected beyond 21 mm, all sound measured at the transducer surface from 5 cm depth necessarily comes from multi-path reflections from near-field tissue.

Since there are no reflections from the random mirror, $\chi = 0$. Then, in the x-plane, Eqn. 17 reduces to

$$R_{\psi\psi}(\Delta x) = R_{\mathcal{M}\mathcal{M}}(\Delta x) \quad (21)$$

and the spatial coherence of $\mathcal{M}$ can be calculated simply with the measured backscattered field. The left image in Fig. 4 shows the simulated data measured in the transducer plane, then focused and gated at the focal depth (i.e. $\mathcal{M}$). The graph on the right of Fig. 4 shows the spatial coherence of $\mathcal{M}$, or $R_{\mathcal{M}\mathcal{M}}(\Delta x)$. The reverberation clutter signal is completely incoherent as demonstrated by a function that is as close to a delta function as diffraction physics allows (the full-width half-maximum of the spatial coherence function of the incoherent field is 1.1λ).

C. Human tissue

The previous two sections showed idealized cases with either scatterers but no abdominal layer or an abdominal layer but no scatterers. The former had a wide spatial coherence function and the latter a narrow one. A more realistic model of the human body has both types of reflective structures. This composite acoustic map is shown on the left of Fig. 5.

The right plot of Fig. 5 also shows the coherence function measured in three healthy volunteers. The backscattered signal was recorded with a Siemens VF7-3 transducer on a Siemens Antares Ultrasound scanner. The transmit frequency was 4.2 MHz and the Axius Direct Ultrasound Research Interface (URI) was used to acquire the data [18]. The same signal processing method that was used for the simulated data was used to determine the experimental spatial coherence curves.

The spatial coherence curves on the right of Fig. 5 show that the simulation realistically captures the coherence properties of *in vivo* abdominal tissue. There is a coherent component due to the scatterers and an incoherent component due to reflections from organized tissue structure. The curves are consistent with the interpretation that they are composed of a superposition of the triangle function and delta function. The coherence curves measured for subjects 1 and 3 fall almost entirely within the error bars for the simulated curve. For this particular combination of abdominal model and scatterer impedance, subject 2 has a shape that is similar to the other curves but it falls outside of the simulated standard deviation. However, a simulation with a thicker abdominal layer, which would be a more realistic approximation of subject 2's abdomen, would provide a better match by increasing the relative contribution of the incoherent delta function with respect to the coherent portion. Note that tissue measured for the simulations bears no relation to the *in vivo* tissue. Nevertheless, the spatial coherence curves have similar characteristics. In these curves, the incoherent contribution accounts for correlation values down to 0.6 and the rest of the signal contribution is coherent. The right balance of near-field reverberation and scattering from the focal plane is needed to obtain realistic spatial coherence curves. These results shows that the balance in the simulations is comparable to the balance observed *in vivo* in the human body.

D. Verification of the independence of the backscattered field and the reverberation clutter

To derive Eqn. 16, it was assumed that the acoustic field reflected from the random mirror U_z^{rcfl} was independent from the reverberation clutter $\mathscr{M}(x, y)$ that arises from the near-field tissue layer. In this model, the scatterer distribution in the imaging plane near the depth $z = F$ is random, and the tissue near depth $z = 0$ is determined by the abdominal structures. The fields in these two different regions are therefore independent.

The validity of Eqn. 16 with respect to this assertion can be verified with independent simulations that perform the addition on the right hand side and that show that the two terms are in fact separable. The autocorrelation of the total field, corresponding to the left hand side of Eq. 17, was shown in the previous section, section V-C, and is plotted as the solid line in Fig. 5. The autocorrelation of a field of backscattered from a random mirror, corresponding to the first term on the right hand side, was shown in section V-A, and the autocorrelation of reverberation clutter, corresponding to the second term on the right hand side, was shown in section V-B. What remains is to add the terms on the right hand side of Eq. 16 to demonstrate the equality with the left hand side. In other words, the addition of the right hand terms of Eqn. 16 are therefore equivalent to the addition of the spatial coherence curves in Figs. 3 and 4, i.e. the coherent triangle function and the incoherent delta function.

As per Eqn. 2 the spatial coherence curves in Figs. 3 and 4 are normalized to one. To undo this normalization and to perform the addition operation with the correct scaling, the relative weight of the delta and triangle functions was determined by the total backscattered amplitude over the time gated window. For reverberation clutter, the weight is given by $\sqrt{\int\int \mathscr{M}^2(x,t)dtdx}$, and for the single backscattered field, it is given by $\sqrt{\int\int \psi^2(x,t)dtdx}$. Losses due to propagation in tissue were taken into account in the reverberation term. This addition of right hand side terms is shown as the dashed curve in Fig. 6. The solid curve in

Fig. 6 was calculated with the total field, which is on the left hand side of Eq. 16 (note that it is identical to the simulated spatial coherence curve in Fig. 5).

The two curves are almost superimposed and there are only slight differences due to minor variations in the fields. Note that Eqn. 16 is valid for *ensemble averages* and not the fields themselves. This shows the spatial coherence of the signal received by an ultrasound transducer is composed of the sum of a coherent backscattered signal from the focal plane and an incoherent reverberation clutter signal. The contribution of each component is proportional to the amplitude of the signal from each region. The relative amplitude of each component as a function of space can be used to characterize spatial coherence imaging, as discussed below.

E. Reverberation in tissue and its influence on spatial coherence

As the reverberation in the tissue layers changes it has an influence on the shape of the spatial coherence curves. This can be achieved in simulation by modulating the impedance mismatch of the near field tissue layer. Fig. 7 shows the spatial coherence curves for impedance mismatches that range between 0% and 200% of the background tissue impedance. At 0% impedance there is no effective tissue layer, at 100% the tissue layer has the original impedance values, and at 200% the tissue layer has twice the measured impedance. At low impedance mismatches, less energy is trapped in between the tissue layers compared to what is backscattered from the focus. Conversely, for large mismatches there is relatively more reverberation signal. This can be observed in the shape of the spatial coherence curves. For low impedance mismatches, the curves are wider because they have a more significant coherent contribution from the diffuse scatterers. For large mismatches, the curves are narrower because there is more incoherent reverberation clutter.

Another way to influence the shape of the spatial coherence curve is to change the coherence properties of the signal backscattered from the focal zone. This can be achieved by focusing in different areas, which alters the ratio of the coherent to incoherent echo amplitude according to the area being examined. This method is presented in the context of diagnostic imaging in the following section.

VI. Spatial coherence imaging

Conventional B-mode imaging is a measure of the impedance mismatch in tissue. In spatial coherence imaging, the image brightness is a measure of the relative contribution of the spatially incoherent component of a received signal (the delta function), to the coherent component (the triangle). This section compares these two imaging methods by considering the image quality of an anechoic lesion.

The tissue model is shown on the left of Fig. 8. There is a near field tissue layer and randomly distributed scatterers. A 5 mm anechoic lesions at 5 cm of depth was modeled by creating a region without scatterers. The signal backscattered from the focus can therefore include regions with or without scatterers.

To generate the RF signals for both imaging methods, the simulated transducer was mechanically translated across the acoustic representation of the human abdomen and 72 independent pulse-echo simulations were performed. Each simulation follows the same physical process as conventional imaging. The focused acoustic wave is transmitted by the transducer surface, it propagates through tissue, is reflected by tissue structure and subresolution scatterers, travels back to the transducer, and it is recorded for further processing.

The same data measured at the transducer position (at depth z=0) was used to generate the conventional B-mode and spatial coherence images. A dynamic focusing delay was applied for each depth at which the spatial coherence function was calculated. The correlation value was integrated between a lag of zero and $\lambda/2$, corresponding to 3.1% of the transmit aperture, to determine average area under the delta function, which then yields the brightness scale. Note that for shallow depths the spatial coherence image appears to be dark because the broad transmit beam is coherent but it is reflected by random scatterers in the near field. Unlike the signal coming from the focus it and hasn't propagated a sufficient distance to become partially coherent. Also note that the theory remains valid for small F/#s (e.g. at shallow depths). There is a departure from the assumptions used in the derivation when the F/#s become large and the beamwidth becomes comparable to the aperture size.

A classical B-mode image, calculated by beamforming each individual simulation into a constant F/# A-line, is shown in the middle image of Fig. 8 with a dynamic range of 70 dB. A short lag spatial coherence image is shown on the right on a linear scale, with average correlation values varying between 0.05 and 0.9. In these images, both the near-field abdominal layer and the anechoic lesion at 5 cm are clearly visible.

The contrast to noise ratio (CNR) is a measure of image quality that is independent of the image brightness. It is based on mean signal intensity in the lesion, S_i, and outside the lesion, S_o, normalized by the standard deviation inside, σ_i and outside σ_o. It can be written as

$$\mathrm{CNR}=\frac{|S_i - S_o|}{\sqrt{\sigma_i+\sigma_o}} \quad (22)$$

The lesion CNR for the conventional B-mode image is 1.21 and for the spatial coherence image the CNR is 1.95. To preserve the same beam characteristics, the region outside the lesion was calculated in the focal zone at a depth of 5 ± 0.25 cm. The CNR in the simulated images is thus in agreement with clinical results that demonstrate that spatial coherence imaging improves lesion detectability [12], [13]. The physical origin for the CNR observed in spatial coherence imaging can be explained by close examination of the spatial coherence curves.

Fig. 9 shows the average spatial coherence curve inside the lesion as a solid line and outside the lesion as a dashed line. Since there are no scatterers in the lesion, the signal received by the transducer is due primarily to reverberation clutter and, to a lesser extent, off-axis scatterers. As was shown in section V-B this signal is incoherent and its spatial coherence function is narrow. Outside of the lesion, the signal received by the transducer comes from reverberation clutter *and* the focal plane, which is equivalent to the tissue model in section

V-C. The image is therefore a measure of the size of the delta function relative to the triangle in the spatial coherence function, and it displays the relative importance of the coherent backscattered field to the incoherent backscattered field. The degree of coherence of the backscattered field, in turn, depends on the reverberating properties of the near-field tissue and on the distribution and amplitude of the reflectors in the focal zone.

VII. Discussion and Conclusion

The spatial coherence of a wave field as it propagates through tissue has been described with theory, simulation, and experiments. This analysis has shown how the spatial coherence measured at the transducer surface depends on the reverberations from the wavelength-size structures in the near-field tissue layer and the backscattered field from the sub-wavelength scatterers in the imaging plane. The reverberation clutter is equivalent to acoustic noise and it decorrelates rapidly. Therefore, its contribution to the total spatial coherence curve is similar to a delta function. Note that this is unlike the slow decorrelation due to phase aberration [7]. The signal backscattered from random scatterers has a wide spatial coherence function that depends on the transducer shape and pulse characteristics. Its contribution to the total spatial coherence function is similar to a triangle function for a rectangular transducer. The ratio of coherent to incoherent signal can be used to define spatial coherence imaging.

The applications of this research extend to any area of ultrasound where reverberation clutter has a significant impact. In areas of the body where there are diffuse homogeneous scatterers, such as the liver or the thyroid, the spatial coherence curves can be used directly to estimate the *in vivo* magnitude of the backscattered signal to reverberation noise. These estimates can be used to calibrate motion filters [19], to estimate jitter in motion estimates [20], and to assess the viability of quantitative estimates of tissue properties.

Acknowledgments

This work is supported by NIH grants R01-EB013661, R01-EB015506, and R01-EB017711. The authors wish to thank the Ultrasound Division at Siemens Medical Solutions USA, Inc. for their in-kind and technical support.

Appendix: Approximate expressions for the backscattered field ψ and the autocorrelation $R_{\psi\psi}$

A. Propagation from 0 to z

Although imaging ultrasound pulses are typically broadband, the propagating wave is separated into its constituent single frequency components, ω, so that Fourier acoustics can be used to describe the propagation physics. Eqn. 3 can subsequently be used to re-establish the broadband spatial coherence characteristics.

Within the Fresnel approximation, the propagation from the source plane to some depth z can be calculated with the propagation operator:

$$h_z(x,y)=e^{jkz}/j\lambda z e^{j(\pi/\lambda z)(x^2+y^2)} \quad (23)$$

Propagation over the distance z can be written as the convolution of the wavefield $U_0(x, y)$ by $h_z(x, y)$. For the aperture defined in Eqn. 8 and for a monochromatic wave, the field in the array plane ($z = 0$) is

$$U_0(x,y)=T(x,y)e^{-j\omega t} \quad (24)$$

Then the field in the $x - y$ plane at a depth z, defined in terms of the spatial variables X and Y, can be written in terms of a convolution using the Fresnel diffraction integral

$$U_z(X,Y)=U_0(X,Y)\underset{XY}{**}h_z(X,Y) \quad (25)$$

and the expansion of this convolution is

$$U_z(X,Y)=\frac{1}{j\lambda z}e^{j(kz-\omega t)}e^{j(\pi/\lambda z)(X^2+Y^2)}\int\int T(x,y)e^{j(\pi/\lambda z)(x^2+y^2)}e^{-2\pi j(Xx+Yy)/\lambda z}dxdy \quad (26)$$

A modified transmittance function $\tilde{T}(x, y)$ can be defined as:

$$\tilde{T}(x,y)=T(x,y)e^{j(\pi/\lambda z)(x^2+y^2)}=O(x,y)A(x,y)\exp\left[j\frac{\pi(x^2+y^2)}{\lambda}\left(\frac{1}{z}-\frac{1}{F}\right)\right] \quad (27)$$

Let $z = F$, then the exponential in Eqn. 27 is zero and $\tilde{T}(x, y) = O(x, y)A(x, y)$. Furthermore, if there is no phase or amplitude aberration, then $A(x, y) = e^{j0} = 1$ and $\tilde{T}(x, y) = O(x, y)$, which is the original aperture function without any phase terms.

By dropping the phase propagation term $e^{j(kz-\omega t)}$, the Fourier transform in Eqn. 26 can be expressed in terms of Eqn. 27:

$$U_z(X,Y)=\frac{1}{\lambda z}e^{j(\pi/\lambda z)(X^2+Y^2)}\mathrm{FT}_{2\mathrm{D}}\{\tilde{T}(x,y)\}_{(X/\lambda z,Y/\lambda z)} \quad (28)$$

where the Fourier transform is taken at the spatial frequencies $X/\lambda z$ and $Y/\lambda z$.

B. Reflection from depth z

The field at the imaging plane is reflected at depth z by the reflectivity function $\chi(X, Y)$ so that

$$U_z^{\mathrm{refl}}(X,Y)=\chi(X,Y)U_z(X,Y) \quad (29)$$

U_z^{refl} represents the field propagating from the imaging plane back to the transducer, i.e. from z to 0. It can be written as

$$U_z^{\mathrm{refl}}=\frac{1}{\lambda z}e^{j(\pi/\lambda z)(X^2+Y^2)}\chi(X,Y)\mathrm{FT}_{2\mathrm{D}}\{\tilde{T}(x,y)\}_{(X/\lambda z,Y/\lambda z)} \quad (30)$$

References

1. Goodman JW. Statistical optics. New York, Wiley-Interscience, 1985, 567. 1985; 1
2. Zernike F. The concept of degree of coherence and its application to optical problems. Physica. 1938; 5(8):785–795.
3. Mallart R, Fink M. The van Cittert–Zernike theorem in pulse echo measurements. J. Acoust. Soc. Am. 1991; 90:2718.
4. Derode A, Fink M. The notion of coherence in optics and its application to acoustics. European journal of physics. 1994; 15(2):81.
5. Goodman, JW. Introduction to Fourier Optics. McGraw-Hill; 1996.
6. Johnston P, Miller J. Phase-insensitive detection for measurements of backscattered ultrasound. IEEE Trans. Ultrasonics Ferroelect. Freq. Control. 1986; 33(6):713–721.
7. Walker W, Trahey G. Speckle coherence and implications for adaptive imaging. J. Acoust. Soc. Am. 1997; 101:1847. [PubMed: 9104014]
8. Mallart R, Fink M. Adaptive focusing in scattering media through sound-speed inhomogeneities: The van Cittert Zernike approach and focusing criterion. Acoustical Society of America Journal. 1994; 96:3721–3732.
9. Szabo, TL. Diagnostic ultrasound imaging. Elsevier Academic Press; 2004.
10. Derode A, Fink M. Spatial coherence of ultrasonic speckle in composites. Ultrasonics, Ferroelectrics and Frequency Control, IEEE Transactions on. 1993; 40(6):666–675.
11. Derode A, Fink M. Correlation length of ultrasonic speckle in anisotropic random media: Application to coherent echo detection. J. Acoust. Soc. Am. 1998; 103:73.
12. Lediju M, Trahey G, Byram B, Dahl J. Short-lag spatial coherence of backscattered echoes: imaging characteristics. Ultrasonics, Ferroelectrics and Frequency Control, IEEE Transactions on. 2011; 58(7):1377–1388.
13. Dahl JJ, Jakovljevic M, Pinton GF, Trahey GE. Harmonic spatial coherence imaging: An ultrasonic imaging method based on backscatter coherence. Ultrasonics, Ferroelectrics and Frequency Control, IEEE Transactions on. 2012; 59(4):648–659.
14. Pinton G, Dahl J, Rosenzweig S, Trahey G. A heterogeneous nonlinear attenuating full-wave model of ultrasound. IEEE Trans. Ultrason., Ferroelec., Freq. Contr. 2009 Mar; 56(3):474–488.
15. Mast TD, Hinkelman LM, Orr MJ, Sparrow VW, Waag RC. Simulation of ultrasonic pulse propagation through the abdominal wall. J. Acoust. Soc. Am. 1997; 102:1177–1190. [PubMed: 9265762]
16. Pinton GF, Trahey GE, Dahl JJ. Sources of image degradation in fundamental and harmonic ultrasound imaging: a nonlinear, full-wave, simulation study. Ultrasonics, Ferroelectrics and Frequency Control, IEEE Transactions on. 2011; 58(6):1272–1283.
17. Derode A, Fink M. Partial coherence of transient ultrasonic fields in anisotropic random media: Application to coherent echo detection. J. Acoust. Soc. Am. 1997; 101:690.
18. Ashfaq M, Brunke S, Dahl J, Ermert H, Hansen C, Insana M. An ultrasound research interface for a clinical system. Ultrasonics, Ferroelectrics and Frequency Control, IEEE Transactions on. 2006; 53(10):1759–1771.
19. Bjaerum S, Torp H, Kristoffersen K. Clutter filters adapted to tissue motion in ultrasound color flow imaging. Ultrasonics, Ferroelectrics and Frequency Control, IEEE Transactions on. 2002; 49(6):693–704.
20. Pinton G, Dahl J, Trahey G. Rapid tracking of small displacements with ultrasound. Ultrasonics, Ferroelectrics and Frequency Control, IEEE Transactions on. 2006; 53(6):1103–1117.

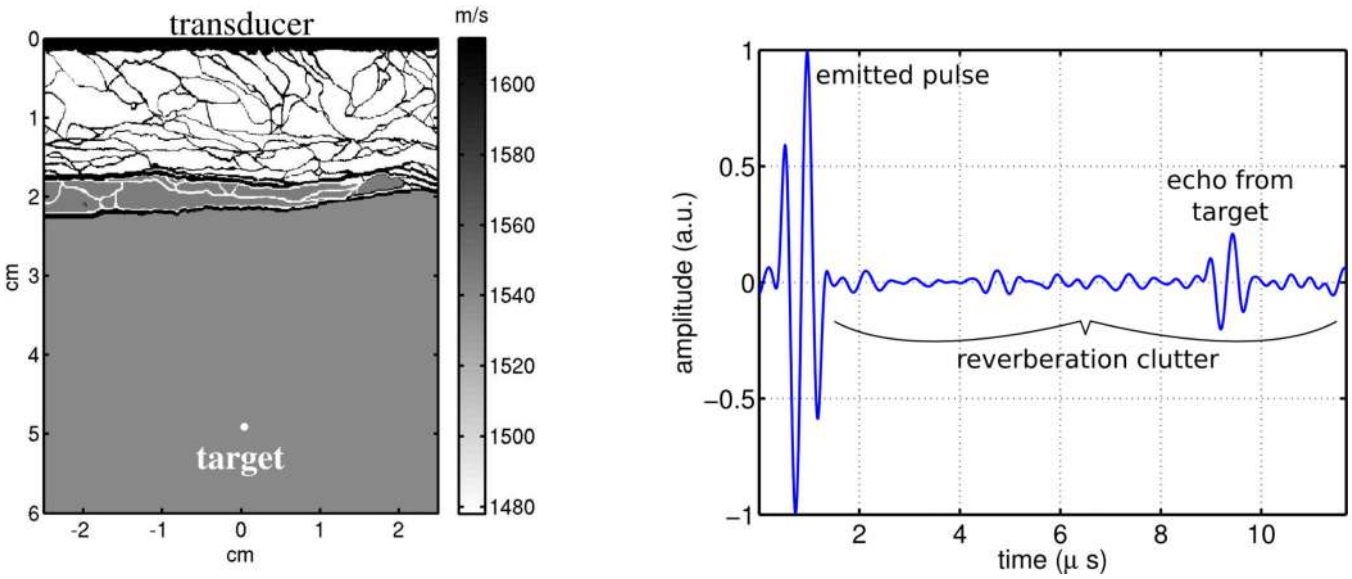

Fig. 1.

The speed of sound map derived from a histological characterization of the human abdomen (left) [15]. A schematic representation of a pulse echo measurement (right) that includes reverberation clutter.

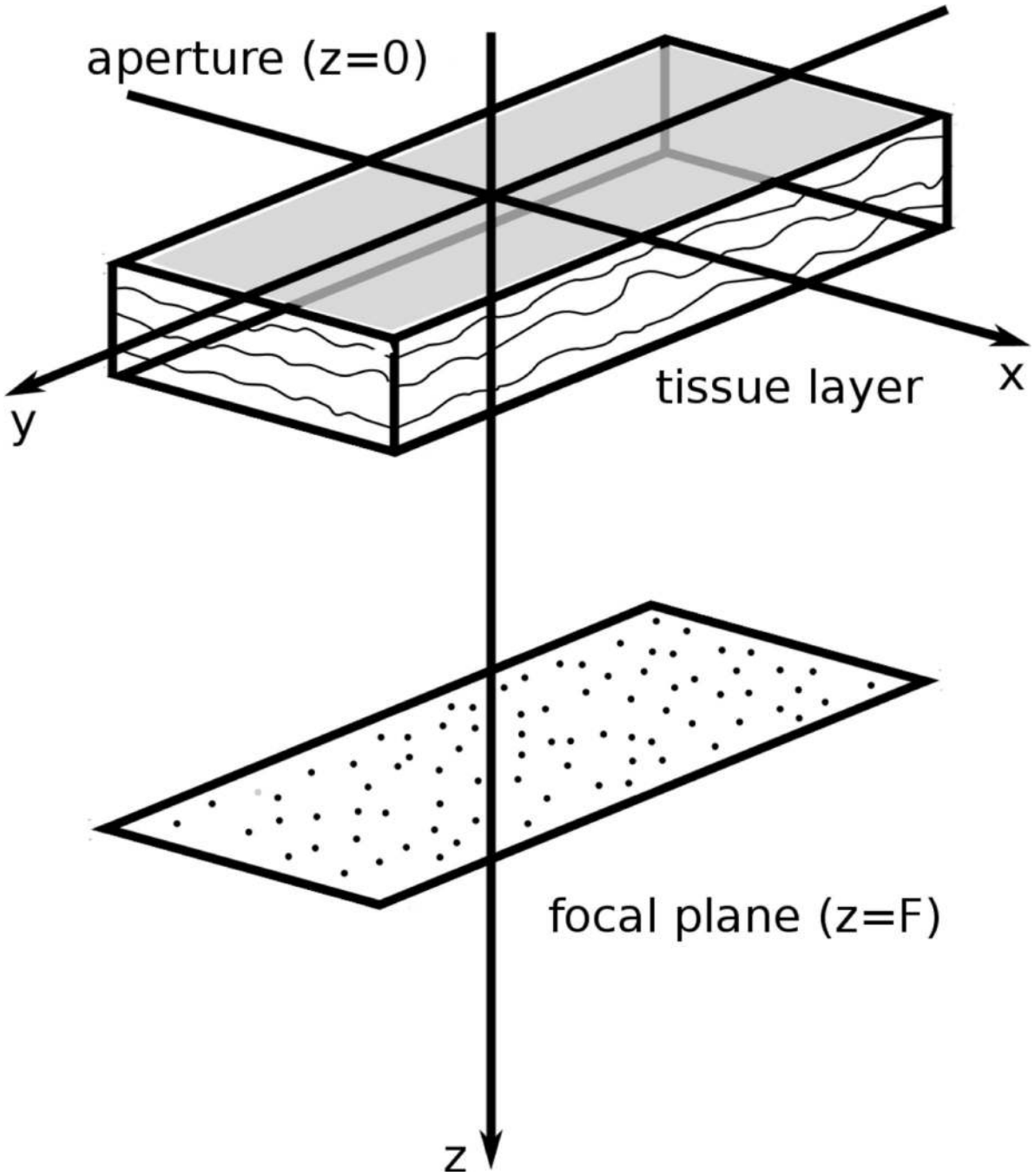

Fig. 2.

A schematic of the model of human tissue used in the spatial coherence theory. A thin near-field tissue layer located just below the transmitting and receiving aperture (at z=0). Random scatterers are in the focal plane (at z=F).

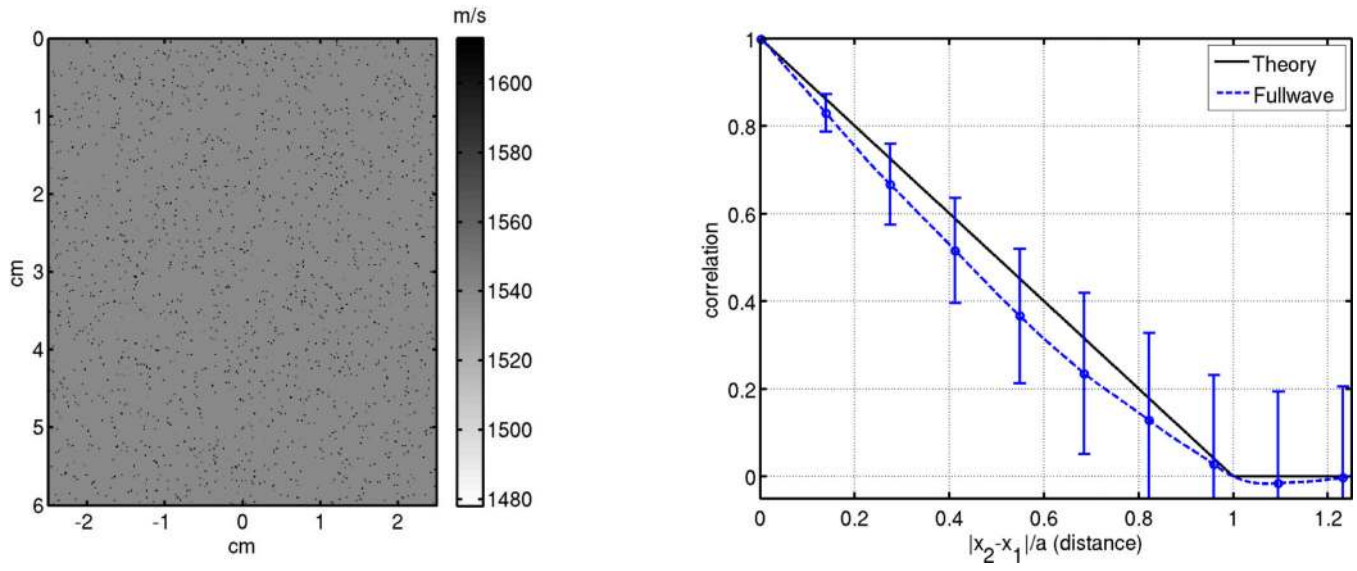

Fig. 3.

The image on the left shows a field of randomly distributed scatterers and the plot on the right compares theoretical predictions with the Fullwave simulation. (Note that since the scatterers are too small to be seen only some scatterers appear for illustrative purposes). The interelement correlation is shown the y-axis and normalized interelement distance on the x-axis. Note that at x=1 the interelement distance is equal to the aperture size. The simulations agree with the theoretical predictions of the VCZ theorem (Eqn. 20).

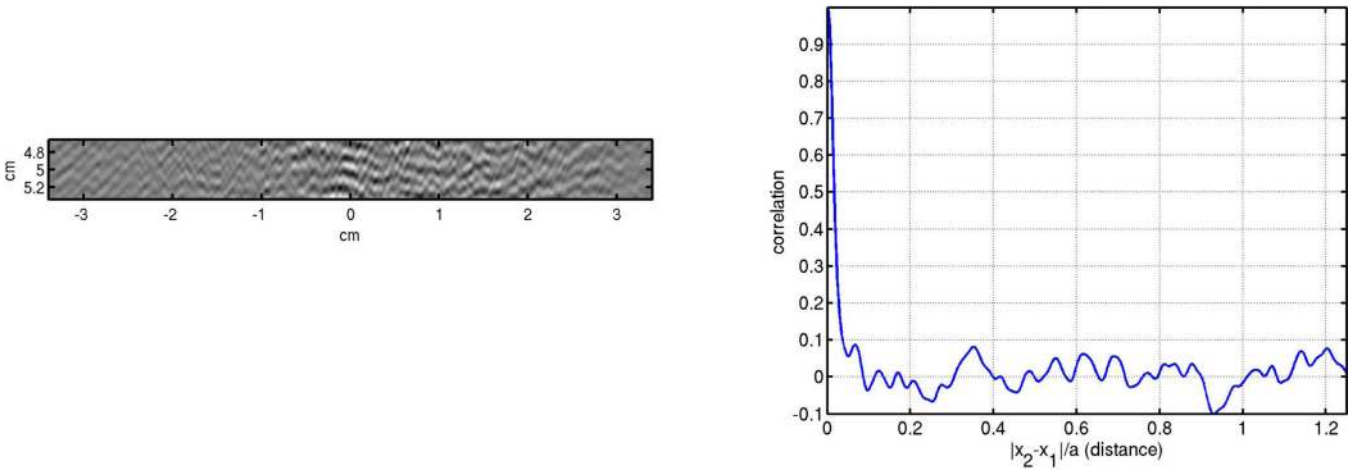

Fig. 4.

The focused, gated wave field measured at the z = 0 plane for a human abdomen without subresolution scatterers simulated in the Fullwave simulation (left). The spatial coherence function of this field (right). Note that at x=1 the interelement distance is equal to the aperture size.

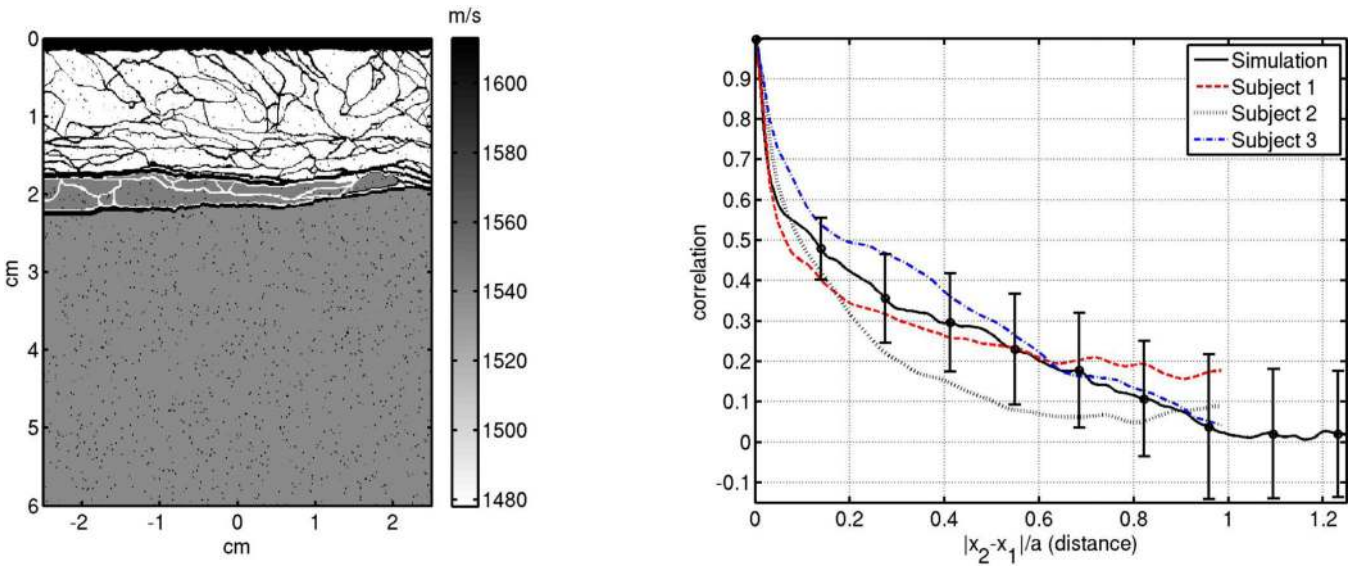

Fig. 5.

A realistic model of the acoustic field in the human body consists of the abdominal layer and subresolution scatterers (shown left). This model compares favorably with the *in vivo* spatial coherence of the backscattered signal from the abdomen of 3 volunteers (right). Theses spatial coherence curves have both a coherent component from the focal plane, and an incoherent component from the near-field reverberation.

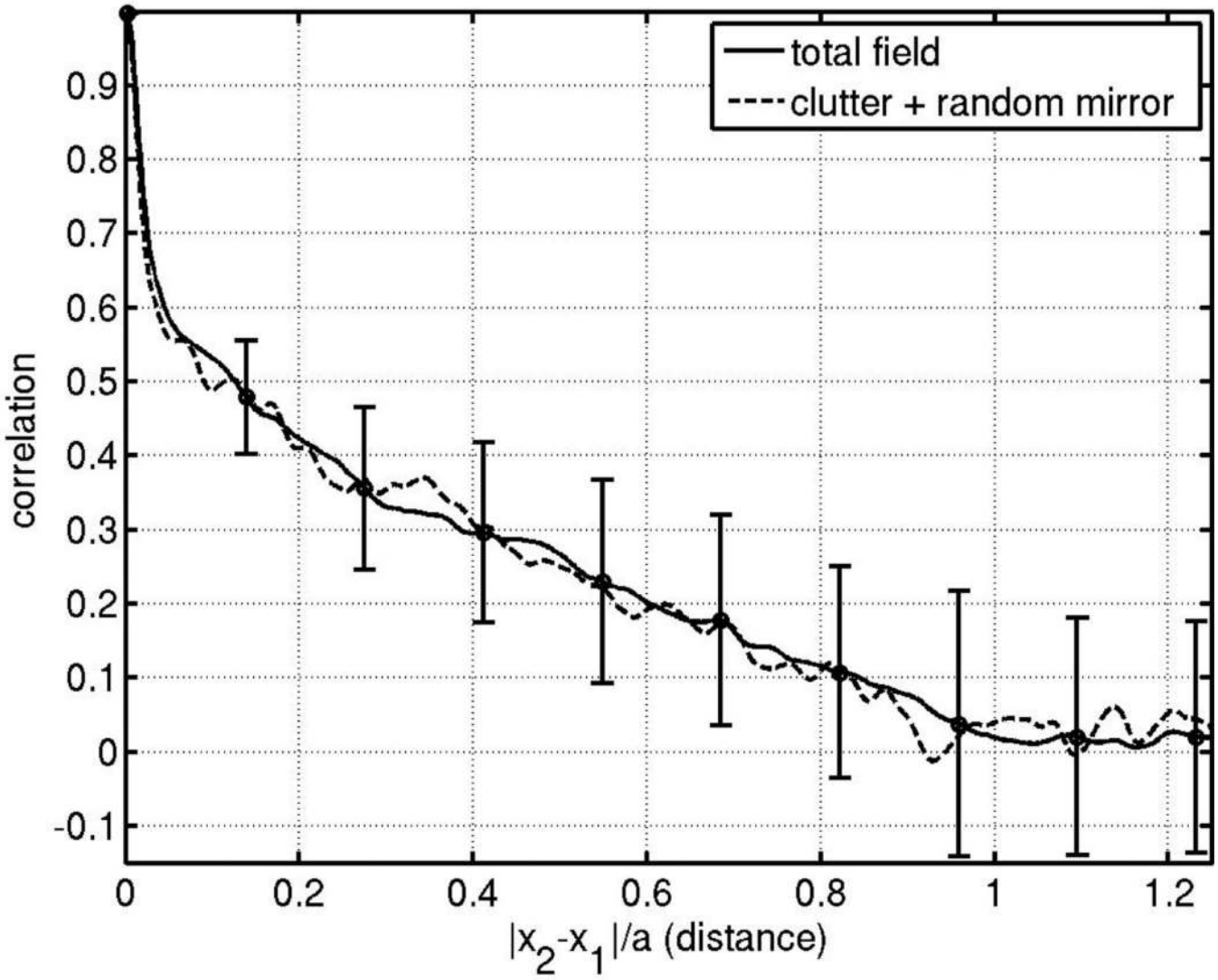

Fig. 6.

The spatial coherence of the simulated backscattered field from the abdominal model with subresolution scatterers (solid). The addition of the simulated spatial coherence curves of the abdomen and the scatterers (dashed). This shows that the autocorrelation of the total field is equal to the addition of the incoherent reverberation to the coherent focal fields.

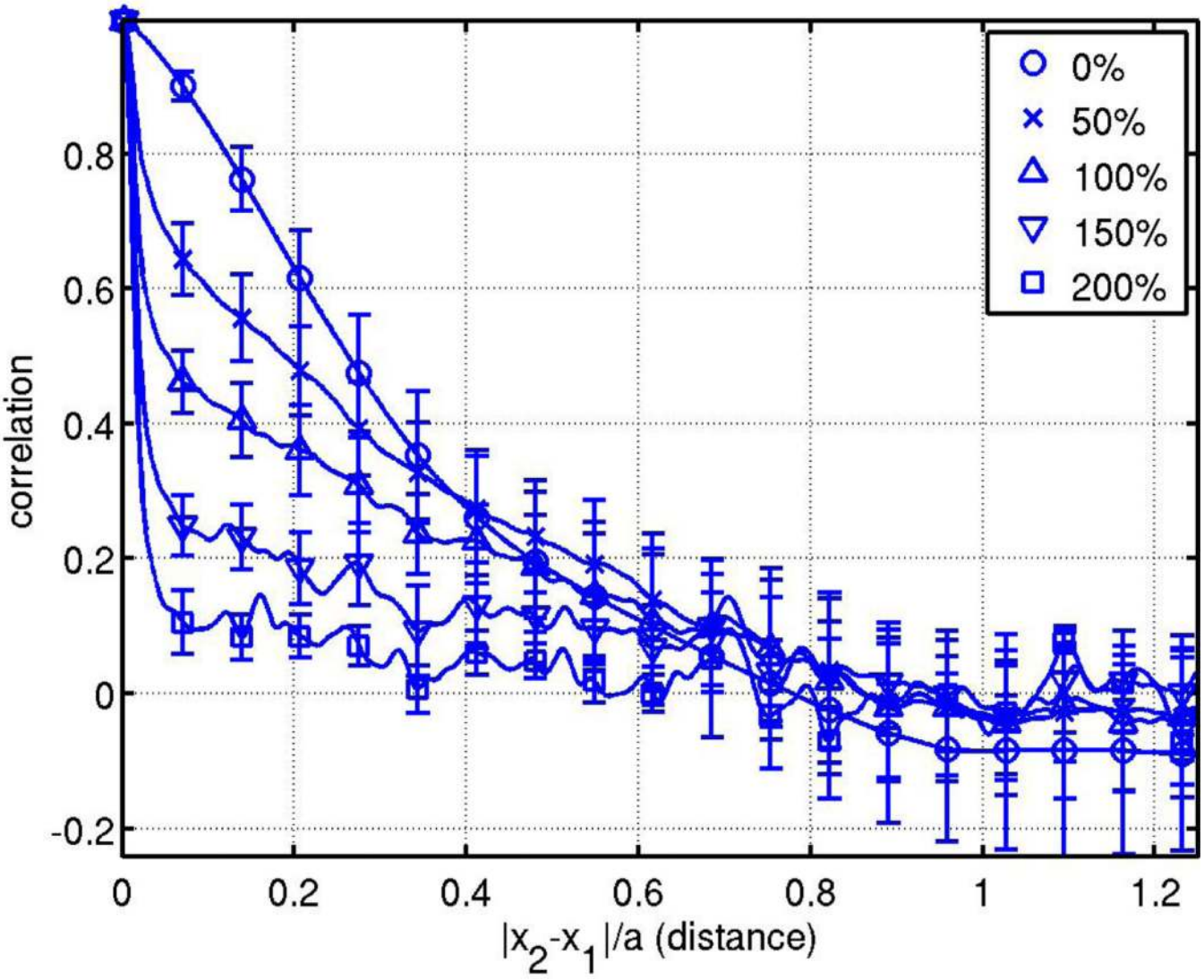

Fig. 7.

Spatial coherence curves for different artificially modulated impedance mismatch of the near-field tissue layer. At 0% impedance there is no tissue layer, at 100% the tissue layer has the original impedance values, and at 200% the tissue layer has twice the measured impedance. The incoherent contribution increases with reverberation.

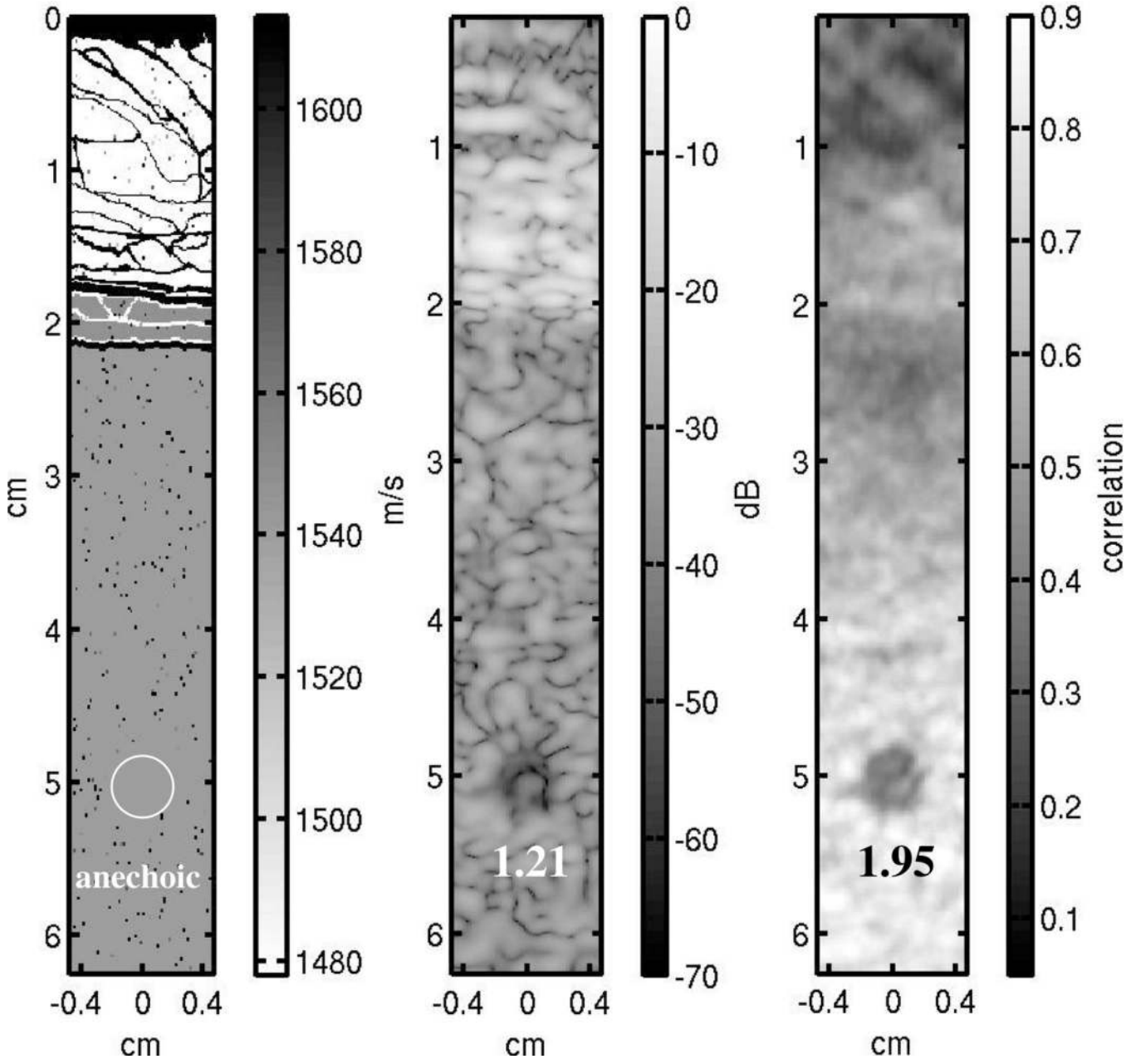

Fig. 8.

The speed of sound map for the abdominal layer, with subresolution scatterers, and an anechoic lesion at the 5 cm focus (left). Corresponding conventional B-mode image (middle) with a lesion CNR of 1.21. Short-lag (λ/2) spatial coherence image (right) with a lesion CNR of 1.95.

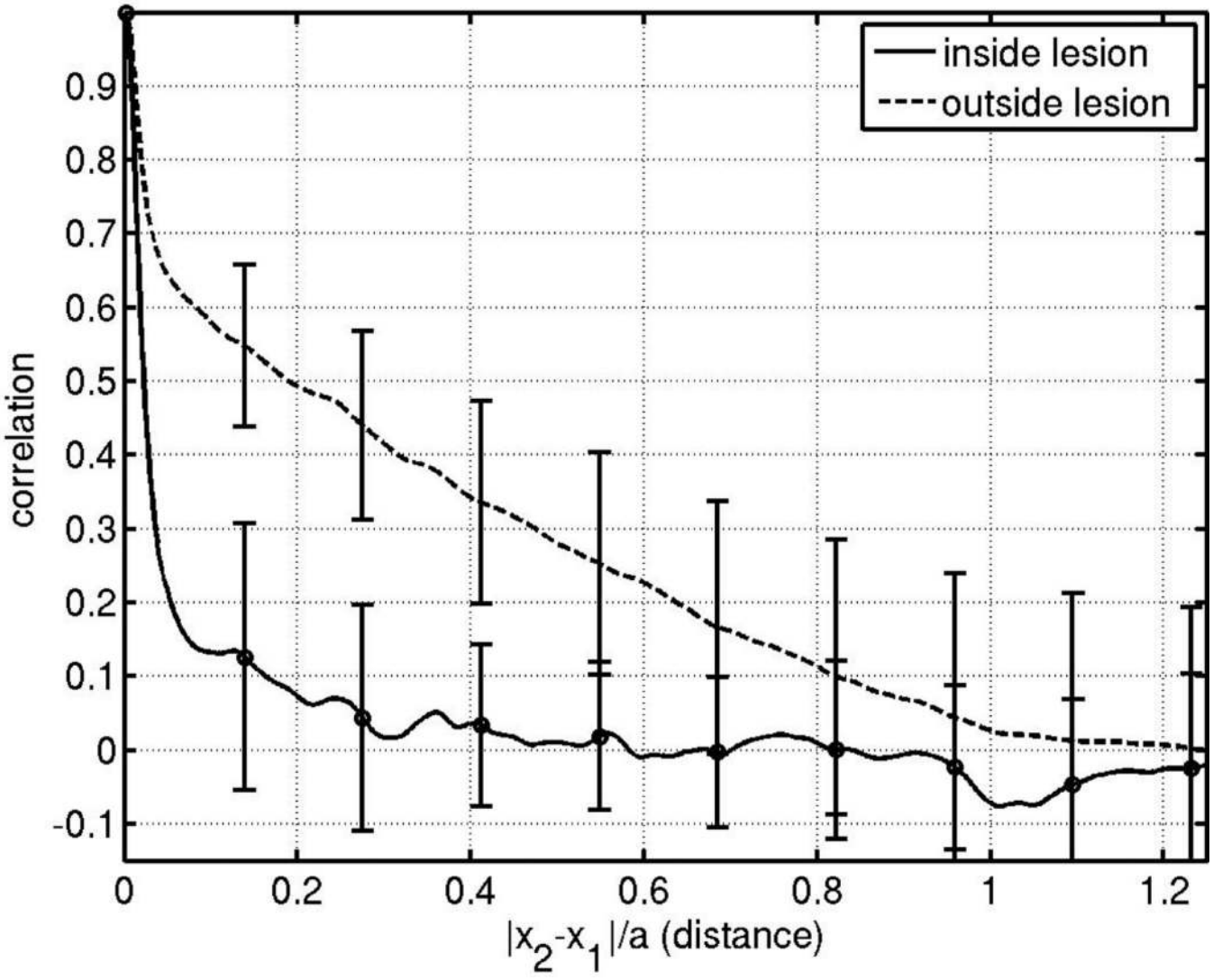

Fig. 9.

The average spatial coherence inside and outside the lesion in Fig. 8, demonstrating the different contributions of the coherent and incoherent components depend on the scatterers in the imaging plane. The interior of the lesion, where the are no scatterers, has a stronger incoherent contribution.

TABLE I

List of symbols and notation

λ	Wavelength
z	Propagation axis
x, y	Coordinates in $z = 0$ plane
X, Y	Coordinates in the imaging plane, z
F	Focal length
$\mathrm{FT}\{\}_{X/\lambda z}$	Fourier transform, $\mathrm{FT}\{\mathrm{T}(\mathrm{x})\}_{X/\lambda z} = \int_{-\infty}^{+\infty} T(x) e^{-2\pi x X/\lambda z} dx$
E	Expected value or statistical average
$R_{\chi\chi}$	Autocorrelation of a random process, $R_{\chi\chi}(x_1, x_2) = E\{\chi(x_1)\chi^*(x_2)\}$
$\underset{x}{*}$	Convolution over the variable x, $f(x) \underset{x}{*} g(x) = \int_{-\infty}^{+\infty} f(\xi) g(x - \xi) d\xi$